Numerical investigations of gap resonance excited by focused transient wave groups

Junliang Gao[1, 2], Hongzhou Chen[3*], Jun Zang[2], Lifen Chen[4], Gang Wang[5], Yazhou Zhu[1]

1. School of Naval Architecture and Ocean Engineering, Jiangsu University of Science and Technology, Zhenjiang 212003, China

2. Research Unit for Water, Environment and Infrastructure Resilience (WEIR), Department of Architecture and Civil Engineering, University of Bath, BA2 7AY, U.K.

3. School of Civil Engineering and Architecture, Northeast Electric Power University, Jilin, 132012, China

4. Faculty of Engineering and Mathematical Sciences, University of Western Australia, Crawley, WA6009, Australia

5. College of Harbour, Coastal and Offshore Engineering, Hohai University, Nanjing 210098, China

Abstract:

Two or more structures arranged side by side with narrow gaps may be suffered from large-amplitude free-surface oscillations, which could cause green water on the deck and lead to dramatic increase of hydrodynamic loading acting on structures. Here, transient resonant motions of the free surface inside a narrow gap between two fixed boxes triggered by focused transient wave groups with various focused wave amplitudes are simulated using a two-dimensional numerical wave tank. The free-surface amplifications not only inside the gap but in the vicinity of the two-box system, the response time and the damping time of the transient gap resonance, the maximum wave loads on both boxes and the relative importance of the higher-order wave loads to the first-order ones are systematically investigated. It is found that the most vulnerable position to green water closely depends on the incident focused wave amplitude. The damping time decreases gradually with increasing focused wave amplitude, while the response time seems insensitive to the latter. As the focused wave amplitude increases, the normalized maximum wave loads on both boxes are also shown to decline gradually overall, while the relative importance of the higher-order wave loads to the first-order ones becomes more and more remarkable.

* Corresponding author. Email: 379988848@163.com (H. Chen)

Keywords: Gap resonance; Focused transient wave group; Wave height amplification; Wave forces; Response time and damping time; OpenFOAM®

1. Introduction

If two or more marine structures are arranged side-by-side in close proximity and are suffered from ocean surface waves, large-amplitude piston-mode motion of the water body inside the narrow gaps between them can happen at certain frequencies, which is commonly referred to as the "*gap resonance*" phenomenon. Gap resonance may trigger very large free surface elevations inside narrow gaps and then may lead to extremely large wave loading on the structures (Miao et al., 2000; Zhu et al., 2005). Hence, in practice, careful considerations should be given to the safe operations of the marine structures deployed side-by-side in close proximity. To further increase the safety of the engineering operations, more research efforts should be made to enhance the understanding of the mechanisms of hydrodynamics related to this phenomenon.

The methodologies adopted in the research field of gap resonance include analytical analyses, physical model experiments and numerical simulations. In the early stage of the research, the analytical analyses were mainly utilized, and basically all the analytical analyses were based on the linear potential flow theory. Based on the linear potential flow theory, Miao et al. (2000) studied the influences of the narrow gaps between multiple floating bodies on wave forces theoretically. Similarly, via solving an eigenvalue equation derived from the linear potential flow theory, Molin (2001) gained an analytical solution for the natural frequencies of different modes inside moonpools of the barges with infinite length and beam. To verify previous analytical analyses and get a better insight of gap resonance, many physical model experiments were further conducted. Saitoh et al. (2006) performed a set of two-dimensional (2D) experiments in a wave tank to investigate the fluid resonance inside a narrow gap formed by two fixed boxes. Tan et al. (2014) conducted 2D physical model tests to study the fluid resonance inside a narrow gap between a fixed box and a vertical wall. Recently, some three-dimensional (3D) physical model experiments were also implemented to simulate the fluid resonance inside the moonpool, between two barges or between the FSPO terminal and the LNG shuttle carrier (e.g., Huang et al. (2020); Li et al. (2016); Zhao et al. (2017)).

To date, most of the numerical investigations utilized the classical potential flow theory combining with the boundary element technique or the scaled boundary finite element technique (e.g., Li et al. (2005); Li and Zhang (2016); Sun et al. (2010); Tan et al. (2019)). However, the studies based on the classical potential flow theory were found to significantly overestimate the wave height amplification inside the gap and the corresponding wave loads on structures. To overcome this shortcoming, several particular techniques have been developed to artificially introduce the wave energy dissipation into the classical potential flow model (e.g., Huijsmans et al. (2001); Ning et al. (2015a, b); Tan et al. (2019)). Thanks to the rapid development of computer technology in the past decade, the Computational Fluid Dynamics (CFD) based numerical simulations have gradually become an effective alternative approach. By using a Navier-Stokes equations model, Lu et al. (2011a); Lu et al. (2011b) investigated the fluid resonance inside narrow gaps between multi-bodies and the corresponding wave forces. Subsequently, based on an open-source CFD package OpenFOAM®, various aspects of the gap resonance problem have been extensively investigated by many scholars (e.g, Chua et al. (2018); Gao et al. (2019b); Jiang et al. (2018)). All these investigations have found that the simulation results gain by the CFD-based models coincide well with the available experimental data.

Although numerous research efforts on gap resonance have been made, the majority of them have focused on the analyses of the steady-state gap resonance excited by regular waves (e.g., Feng and Bai (2015); Gao et al. (2020a); Jiang et al. (2019a); Jiang et al. (2019b); Li (2019)). The studies on the transient gap resonance triggered by focused transient wave groups started relatively late and few researchers focused on this problem. Using a potential flow code DIFFRACT, Taylor et al. (2008) first investigated the fluid response inside the gap between two identical fixed rectangular barges, and only the time series of the free surface elevations inside the gap were simply compared with those of incident focused wave groups. Subsequently, the first- and higher-order components of the resonant fluid response inside the narrow gap between two identical fixed rectangular barges induced by focused wave groups were experimentally studied in Zhao et al. (2017). Recently, by using the OpenFOAM® model, Wang et al. (2018) established a numerical wave tank to accurately reproduce the experiments of Zhao et al. (2017). Based on the numerical results of Wang et al. (2018), both wave and laminar boundary layer scales for the transient gap resonance were further resolved in Wang et al. (2019).

Based on Gao et al. (2019b), it has been found that the achievement of the steady-state gap resonance needs a continuous action of incident regular waves for a long time. However, for real ocean waves, they are usually irregular and transient, and in general it is uneasy to reach steady state in real oceans. Considering the irregular and transient features of real ocean waves and relatively few research efforts, there is a tremendous need to further strengthen the investigation on the transient gap resonance induced by focused transient wave groups. For the few existing studies on the transient gap resonance (i.e., Taylor et al. (2008); Wang et al. (2018); Wang et al. (2019); Zhao et al. (2017)), only the resonant wave climates inside the narrow gap were paid attention to by them. To the best of the authors' knowledge, the wave climates both in front of and at the rear of the multi-body system and the wave loads acting on the structure during the transient gap resonance have not been investigated so far.

In light of this, to further improve the knowledge of related phenomena involved in the transient gap resonance induced by the focused wave groups, this paper mainly focuses on the following three aspects. Firstly, from the viewpoint of the green water on the deck, it is still unknown whether the most dangerous position is always located inside the narrow gap. Hence, it is necessary to first examine the free-surface amplifications not only inside the gap but also in the vicinity of the multi-body system. Secondly, both the response time and the damping time of the transient gap resonance are then estimated quantitatively. In practical applications, the accurate estimation of the response and damping time is vital for the safe evacuation of staff and the reasonable arrangement of operation time during the offloading operations under gap resonance conditions. Finally, considering that a good understanding of wave loading characteristics would help engineers to perform reasonable structural design, the maximum wave loads and the relative importance of the higher-order wave loads to the first-order ones are also investigated. In this article, a system made up of two identical fixed boxes subjected to focused wave groups with various amplitudes is investigated.

In Sections 2, 3 and 4, the numerical model adopted in this paper, the setup of numerical wave flume and the validation of the numerical model against available experimental and numerical data are presented, respectively. The numerical results and discussions are presented in Section 5. Finally, concluding remarks based on the results are drawn in Section 6.

2. Numerical model description

In order to take into account the wave energy dissipation around the gap caused by the fluid viscosity, a CFD-based numerical model is indispensable. All numerical experiments in this article are conducted by adopting OpenFOAM® version 3.0.1. The built-in "*interFoam*" multiphase solver combined with the "*waves2Foam*" toolbox proposed by Jacobsen et al. (2012) is utilized for tracking the interface of air/water, generating and absorbing waves (refer to Fig. 1).

At the inlet boundary, the velocity and the free-surface elevation can be defined as those of a regular wave train or an irregular wave train, and the pressure gradient is set to zero. Two relaxation zones are arranged in the vicinity of the outlet and inlet boundaries to dissipate the transmitted and reflected waves. At the right and bottom boundaries of the wave flume and at the solid walls of boxes, the boundary condition is set as "no-slip". At the upper boundary of the flume, "atmosphere" boundary condition is employed. As per the requirements of OpenFOAM® for a 2D problem, the boundary condition at the front and back boundaries is set to "empty". To ensure obtaining accurate and stable numerical results, the largest Courant number in all simulations is set to 0.25.

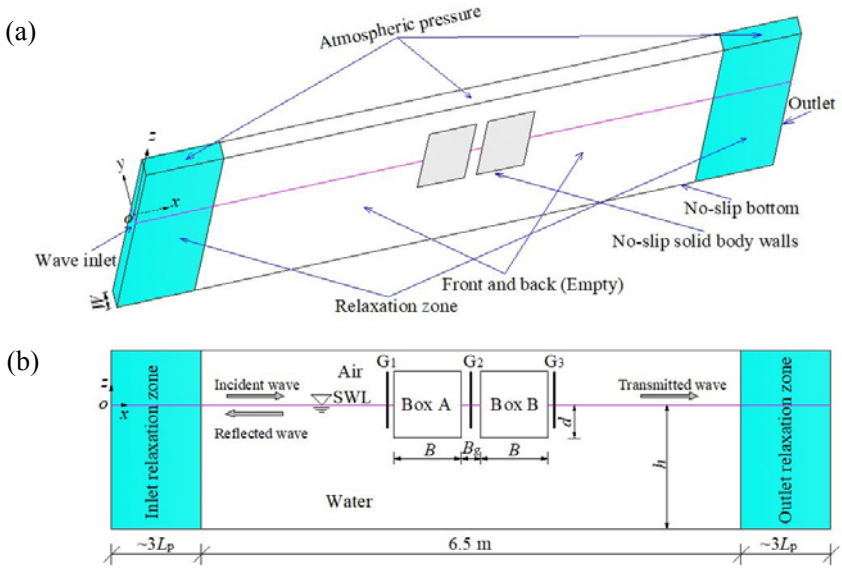

Fig. 1. Definition sketch of the numerical wave flume: (a) the coordinate system and boundary conditions; (b) definitions of geometric parameters and positions of wave gauges.

It should be emphasized that the wave loads studied in this article refers to those excited by

the hydrodynamic pressure (that is, the static buoyancy is excluded) and that the moments on the two boxes correspond to their respective centroids.

3. Numerical wave flume

Fig. 1 presents the setup of the 2D numerical wave flume utilized in all simulations. The coordinate system (o, x, y, z) is defined as follows: the origin is situated at the still water level (SWL) of the inlet boundary, the x-axis is in the wave propagation direction, the y-axis is in the width direction of the flume and the z-axis is in the upward direction. The numerical wave flume is 18.5 m long and 0.8 m high, and its width is W=0.01 m that corresponds to a computational cell. Two fixed boxes with identical size and draft are arranged at the middle of the flume. The height, breadth and draft of each box are H=0.5 m, B=0.5 m and d=0.25 m, respectively. The depths of the air and water zones are h_a=0.3 m and h=0.5 m, respectively. The gap width between boxes is B_g=0.05 m.

These configurations are consistent with the laboratory experiments conducted in Saitoh et al. (2006) and the numerical studies in Lu et al. (2011b). In these two papers, only the steady-state gap resonance induced by regular waves was investigated. Based on their studies, it has been found that the fluid resonant frequency inside the gap shown in Fig. 1 is kh=1.556, or equivalently, ω=5.285 rad/s (k and ω denote the wave number and the angular frequency, respectively). According to the linear dispersion relationship, the wavelength corresponding to the resonant frequency is L_p=2.02 m. Two relaxation zones with identical length are deployed in the numerical flume and their length is set to 6.00 m, approximately triple the wavelength corresponding to the resonant frequency. To record the wave climates both inside the gap and in the vicinity of the two-box system, three wave gauges are arranged in such a way that G_2 is in the middle of the gap and both G_1 and G_3 are very close to the upstream/downstream of the two-box system with only the distance of 0.01 m from the edge of each box.

In this article, the NewWave-type focused wave group proposed by Tromans et al. (1991) is employed. The focused wave group consists of many individual cosine wave components that focus at a specific point in time and space. According to the linear wave theory, for a unidirectional focused transient wave group, the free-surface elevation at any time and any spatial location can be expressed as:

$$\eta(x,t)=\sum_{n=1}^{N}a_n\cos\varphi_n\ , \tag{1}$$

where

$$a_n=A_{\mathrm{f}}\frac{S(\omega_n)\times\Delta\omega}{\sum_{n=1}^{N}S(\omega_n)\times\Delta\omega}, \tag{2}$$

$$\varphi_n=k_n(x-x_{\mathrm{f}})-\omega_n(t-t_{\mathrm{f}})+\varphi_0\ . \tag{3}$$

N denotes the number of all wave components. A_{f} denotes the focused wave amplitude occurring at the focus time and location. a_n, ω_n and k_n respectively denote the wave amplitude, the angular frequency and the wavenumber of the n^{th} wave component, where ω_n and k_n satisfy the linear dispersion relationship. $\Delta\omega$ is the increment of the angular frequency. x_{f} and t_{f} denote the focus location and the focus time, respectively, and they are set to 9.25 m (i.e., the position of gauge G_2) and 10.0 s in all incident focused wave groups. φ_0 is the phase angle of the wave group, and for a crest-focused wave group, φ_0=0 . $S(\omega_n)$ is the wave energy spectrum that describes the wave energy distribution among various wave components.

Identical to Chen et al. (2014), the JONSWAP spectrum proposed by Hasselmann et al. (1973) is utilized, which is expressed as

$$S(\omega)=\alpha g^2\frac{1}{\omega^5}\exp\left[-\frac{5}{4}\left(\frac{\omega_{\mathrm{m}}}{\omega}\right)^4\right]\times\gamma^{\beta}\ , \tag{4}$$

where

$$\beta=\exp\left[-(\omega-\omega_{\mathrm{m}})^2\Big/\left(2\sigma^2\omega_{\mathrm{m}}^2\right)\right], \tag{5}$$

and α is set to 0.0081 empirically, ω is the angular frequency, ω_{m} is the spectral peak angular frequency. σ is the spectral shape parameter, σ = 0.07 when $\omega\le\omega_m$, otherwise σ = 0.09. γ is the peak enhancement factor and the value of 3.3 is chosen here. In the current study, 100 frequency components (i.e., N=100) equally spaced between $0.3\omega_m$ to $3.0\omega_m$ are used to produce the focused transient wave group. To ensure that the transient gap resonance can be triggered, the spectral peak frequency, ω_{m}, of all the focused transient wave groups considered in this paper is set to equal to the fluid resonant frequency (i.e., ω_{m} = 5.285 rad/s). The incident focused wave amplitude, A_{f}, in the absence of boxes gradually increases from 0.01 m to 0.07 m, in an interval of 0.01 m.

To evaluate the relative importance of the higher-order wave loads to the first-order ones, the

four-phase combination method proposed by Fitzgerald et al. (2014) is adopted to separate the harmonic components of the wave loads on both boxes during transient gap resonance. This method has been applied to analyze the harmonic structures of the wave loads on the surface piercing vertical cylinder (Chen et al., 2019; Fitzgerald et al., 2014) and those of the resonant free surface inside a narrow gap between two barges (Zhao et al., 2017). For each crest-focused wave group considered in this article, additional three different NewWave groups are further generated using the same signal, but with each component shifted by a relative phase of $\pi/2$, π or $3\pi/2$, respectively. They correspond to a trough focus and up- and down-crossings. Due to limited space, the detailed theory of the four-phase combination method is not described here, and the interested reader is referred to Fitzgerald et al. (2014).

It should be noted that prior to conducting the simulations of the transient gap resonance, a numerical wave flume in the absence of the two-box system is first used to accurately produce the desired focused wave groups. Because the dispersive focusing approach formulated by Eq. (1) is based on the linear wave theory, it would inevitably result in a shift of the actual focused position and focused wave amplitude due to nonlinear wave-wave interactions (Johannessen and Swan, 2008). In this article, the iterative method proposed by Fernández et al. (2014) is utilized. This approach iteratively corrects both the amplitudes and the initial phases of various frequency components in a wave group, which is expressed as

$$a_{\mathrm{in}}^{k}(\omega_n) = a_{\mathrm{in}}^{k-1}(\omega_n)\, a_{\mathrm{tgt}}(\omega_n) / a_{\mathrm{out}}^{k-1}(\omega_n), \tag{6}$$

and

$$\varphi_{\mathrm{in}}^{k}(\omega_n) = \varphi_{\mathrm{in}}^{k-1}(\omega_n) + \left(\varphi_{\mathrm{tgt}}(\omega_n) - \varphi_{\mathrm{out}}^{k-1}(\omega_n)\right), \tag{7}$$

in which $a_{\mathrm{in}}^{k}(\omega_n)$ and $\varphi_{\mathrm{in}}^{k}(\omega_n)$ denote the amplitude and phase of an input spectral component at angular frequency ω_n, respectively. $a_{\mathrm{out}}^{k}(\omega_n)$ and $\varphi_{\mathrm{out}}^{k}(\omega_n)$ denote the amplitude and phase of the corresponding frequency components of the recorded/measured output spectrum, respectively. The superscript k refers to the k^{th} iteration. $a_{\mathrm{tgt}}(\omega_n)$ and $\varphi_{\mathrm{tgt}}(\omega_n)$ are determined by the pre-selected target spectrum, i.e., Eq. (4). Iteration continues until the simulated focused wave amplitude matches the target one, and various frequency components focus at the desired location in the flume. In fact, the iterative method has been widely used to accurately generate focused wave groups in literature (e.g., Chen et al. (2019); Gao et al. (2020b)).

In general, the simulation results of hydrodynamic problems are broadly influenced by the

mesh employed. To achieve a reliable and accurate solution, some criteria need be met to produce a high quality mesh. A built-in mesh generation utility supplied with OpenFOAM®, "*blockMesh*", is utilized here to produce meshes of hexahedral cells. Typical meshes around the two-box system in the computational domain is presented in Fig. 2. To save the computing cost, non-uniform meshes are employed. Fine meshes with higher resolution are utilized around the two-box system, especially inside the narrow gap. To better track the interface between air and water, the meshes become denser from the atmosphere/bottom boundaries to the SWL. For both the wave flumes with and without the two-box system, all the settings on the meshes are identical except that for the flume with the two-box system the cells inside boxes are further removed by using "*snappyHexMesh*", another built-in utility supplied with OpenFOAM®.

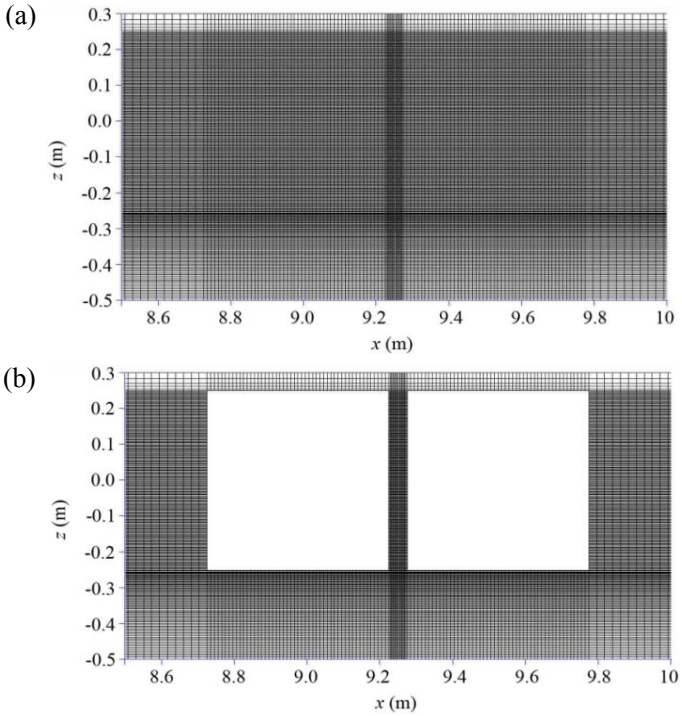

Fig. 2. Typical meshes around the two-box system in the computational domain: (a) the meshes in the absence of boxes; (b) the meshes with boxes.

To examine the influences of various mesh densities on the simulation results, the incident focused wave groups in the absence of the two-box system and the response of the fluid inside the narrow gap between the two boxes are respectively simulated by adopting four different mesh settings, namely Meshes 1-4, with gradually increasing mesh resolutions. For the numerical wave flume without boxes, the numbers of the cells for these four meshes are 124600, 201080, 380660

and 441760, respectively. For the numerical wave flume with the two boxes, the numbers of the cells for the four meshes are slightly less than the corresponding ones of the wave flume without boxes because the cells inside the two boxes are removed.

Fig. 3 demonstrates the comparisons of time seres of free-surface elevations at the focus position (i.e., at gauge G_2) under conditions of Meshes 1-4 for the undisturbed crest-focused wave group with ω_m = 5.285 rad/s and A_f= 0.07 m. It can be seen that there exist slightly differences at the maximum crest and the two adjacent troughs for Meshes 1-3. However, when the mesh resolution further increases, the time series of free-surface elevation for Mesh 4 are shown to be almost identical to those for Mesh 3, which indicates that the convergent results has already been achieved by Mesh 3. Fig. 4 further presents the dependence of the free-surface elevation inside the gap on the mesh resolution for the crest-focused wave group with ω_m = 5.285 rad/s and A_f= 0.07 m when the two-box system exists. Similar to Fig. 3, it is also found that the convergent free-surface elevation inside the gap can be achieved by Mesh 3. Hence, considering the calculation accuracy and efficiency, the configuration of Mesh 3 is employed in all simulations.

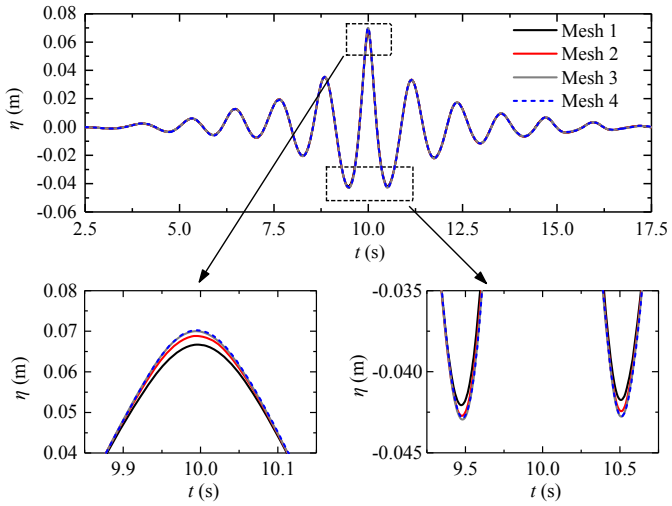

Fig. 3. Dependence of the free-surface elevation at the desired focus position (i.e., at gauge G_2) on the mesh resolution for the undisturbed crest-focused wave group with ω_m = 5.285 rad/s and A_f=0.07 m.

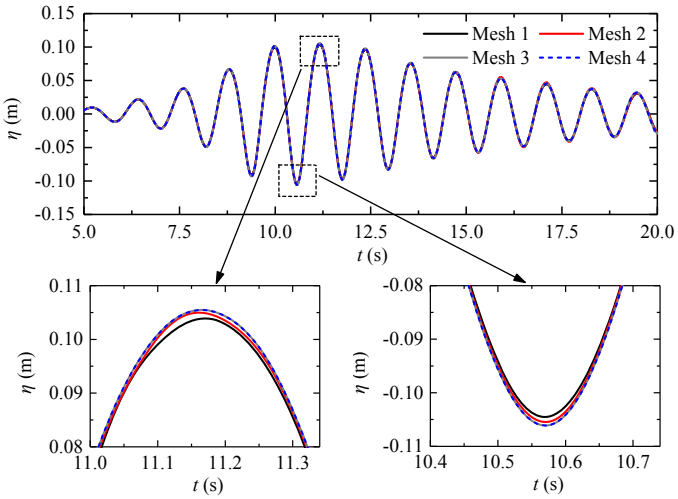

Fig. 4. Dependence of the free-surface elevation at gauge G_2 on the mesh resolution for the crest-focused wave group with ω_m = 5.285 rad/s and A_f = 0.07 m when the two-box system exists.

4. Numerical model validation

Prior to implementing the investigations on the transient gap resonance induced by the focused wave groups, it is essential to validate the reliability of the numerical model and the accuracy of the numerical results under condition of the mesh density adopted (i.e., Mesh 3). Considering that there is a lack of experimental data on the 2D transient gap resonance triggered by focused wave groups so far, the numerical model and the wave flume described in Sections 2 and 3 are verified by comparing the results predicted by OpenFOAM® with available experimental and numerical data for the steady-state gap resonance excited by regular waves. As mentioned in Section 3, the configurations of the two-box system shown in Fig. 1 are identical to those of the laboratory experiments in Saitoh et al. (2006) and the numerical simulations in Lu et al. (2011b), and the steady-state gap resonance triggered by regular waves were considered in them. Hence, in this section, part of the experiments in Saitoh et al. (2006) are reproduced based on the OpenFOAM® model and the numerical wave flume with Mesh 3.

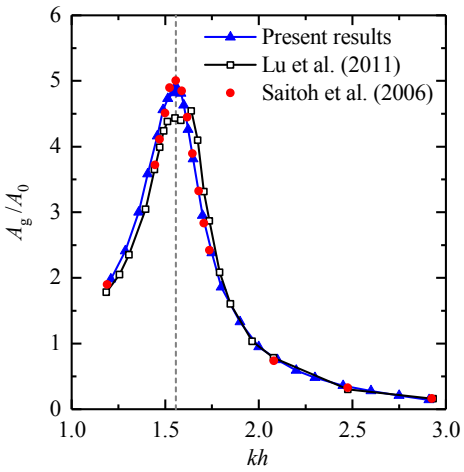

Fig. 5. The amplification curve of the free-surface elevation inside the gap when the two-box system is subjected to regular waves with the amplitude of A_0=0.012 m and various frequencies, in which A_g denotes the wave amplitude inside the gap.

Fig. 5 presents the comparison of the amplification curves of the free-surface elevation inside the gap obtained by the present model, the experimental measurements in Saitoh et al. (2006) and the CFD-based predictions in Lu et al. (2011b) when the two-box system is subjected to regular waves with the amplitude of A_0=0.012 m and various frequencies. A_g in this figure refers to the response wave amplitude inside the narrow gap. It is clear that the free-surface amplifications inside the gap predicted by the present model coincides fairly well with both the experimental data of Saitoh et al. (2006) and the numerical results of Lu et al. (2011b).

Fig. 6 further shows the comparisons of the wave forces on boxes estimated by OpenFOAM® with the CFD-based results in Lu et al. (2011b). For both the horizontal and vertical wave forces, the overall agreement between the present estimations and those in Lu et al. (2011b) can also be observed. These phenomena indicate that when the numerical flume shown in Fig. 1 and the mesh configuration Mesh 3 are adopted, the OpenFOAM® model can obtain the accurate and reliable simulation results for both the fluid amplification and the wave loads during gap resonance.

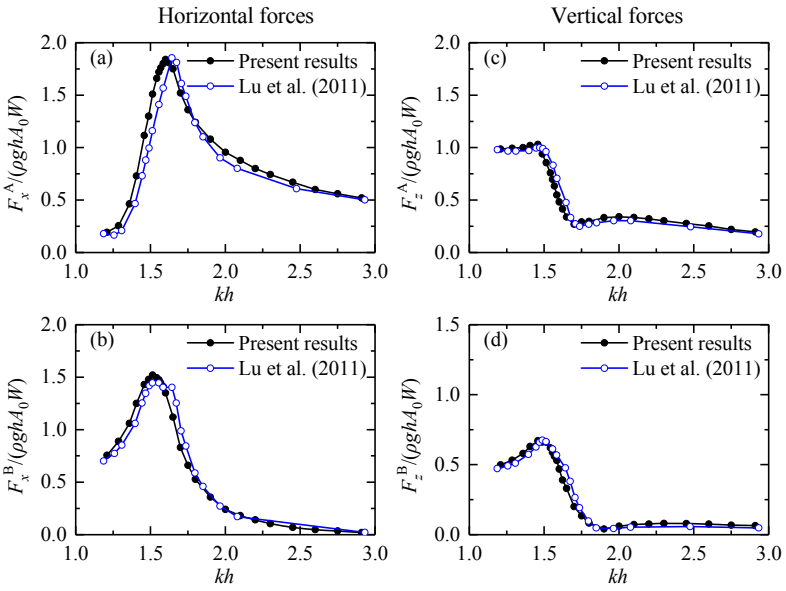

Fig. 6. Comparisons of the wave forces acting on boxes between the present results and the CFD-based results in Lu et al. (2011b). (a) and (b) correspond to the horizontal forces on Boxes A and B, respectively; (c) and (d) correspond to the vertical forces on Boxes A and B, respectively.

5. Numerical results and discussion

In order to obtain a comprehensive understanding of the hydrodynamic characteristics, the amplifications of the free-surface elevations not only inside the gap but in the vicinity of the two-box system are first presented in Section 5.1. Subsequently, the response time and the damping time of the transient gap resonance are discussed in Section 5.2. Then, the maximum wave loads and the relative importance of the higher-order wave loads to the first-order ones are investigated in Sections 5.3 and 5.4, respectively.

5.1 Amplifications of free-surface elevations

To visually present how the existence of the two boxes in close proximity affect the wave climates, the time series of the free-surface elevations at gauges G_1-G_3 excited by focused wave groups with A_f= 0.01 m and 0.07 m under conditions of without and the two-box system are first compared in Fig. 7. Three obvious phenomena can be easily seen. First, for gauge G_1 (see Fig. 7a and d), because of the partial reflection effect of the two-box system, the free-surface elevations with the two boxes ($_1\zeta$) become significantly larger than the corresponding ones without boxes ($_1\eta$), regardless of the incident focused wave amplitude. In addition, the amplification of the

free-surface elevation seems to increase with the increase of the focused wave amplitude. Second, for gauge G_{02} (see Fig. 7b and e), the obvious amplification of the free-surface elevation due to the existence of the two boxes is also clearly seen. However, different from gauge G_1, the amplification of the free-surface elevation at gauge G_{02} seems to decrease with the focused wave amplitude. Besides, compared with the undisturbed incident wave groups ($_2\eta$), the free-surface elevations inside the narrow gap ($_2\zeta$) take more time to build up and then last for a very long time after achieving the maximum oscillations, which coincides with the related finding in Taylor et al. (2008) and Zhao et al. (2017). Third, for gauge G_3 (see Fig. 7c and f), the free-surface elevations with boxes ($_3\zeta$) becomes significantly less than the corresponding ones without boxes due to the shielding effect of the two-box system which acts like a dual-pontoon floating breakwater (e.g., Ji et al. (2016); Zhao and Ning (2018)).

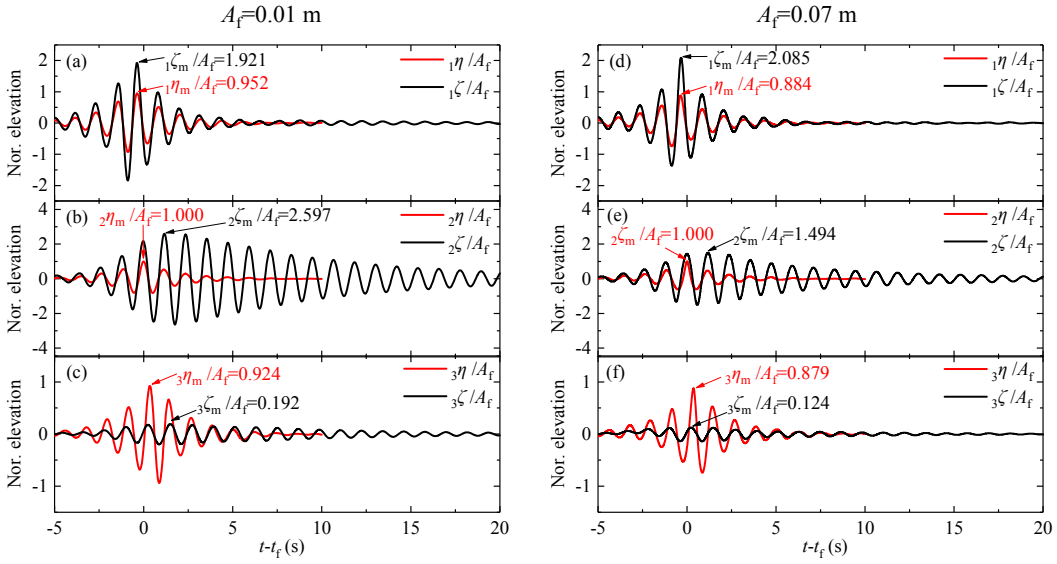

Fig. 7. Comparisons of the time series of the free-surface elevations at gauges G_1-G_3 under conditions of without and the two-box system. $_i\eta$ and $_i\zeta$ denote the free-surface elevation at gauge i (i=1, 2 and 3) under conditions of without and with the two-box system, respectively. The subscript "m" of both η and ζ represents their maximum free-surface elevations. (a)-(c) correspond to the incident crest-focused wave group with A_f=0.01 m, and (d)-(f) correspond to the incident crest-focused wave group with A_f=0.07 m.

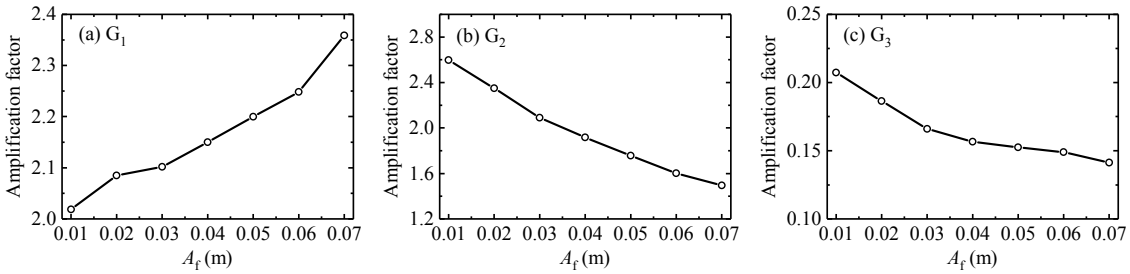

Fig. 8. Variations of the amplification factors of the free-surface elevations at gauges G_1-G_3 with respect to the incident focused wave amplitude. The amplification factor at each gauge is defined as the ratio of ${}_i\zeta_m$ to ${}_i\eta_m$ (i=1, 2 and 3).

To better present the influences of the two-box system on the wave climates, the amplification factors of the free-surface elevations defined as the ratio of ${}_i\zeta_m$ to ${}_i\eta_m$ (i=1, 2 and 3) at gauges G_1-G_3 under conditions of various incident focused wave amplitudes are demonstrated in Fig. 8. For gauge G_1 (see Fig. 8a), the amplification factor of the free-surface elevation increases monotonously with the increase of the focused wave amplitude. While for gauges G_2 and G_3 (see Fig. 8b and c), the former is shown to decease gradually with the latter. From the viewpoint of causing green water on the deck, it is obvious that the transmitted wave group at gauge G_3 has the least possibility because all their amplification factors are very small (less than 0.22). By contrast, the wave climates at gauges G_1 and G_2 present much larger free-surface amplification (larger than 1.49). Hence, there is a greater possibility to occur green water inside the gap or in front of the two-box system.

In order to further assess which position is the most vulnerable to occurring green water, Fig. 9 demonstrates the comparison of the normalized maximum free-surface elevations at gauges G_1 and G_2 under conditions of various incident focused wave amplitudes. It is seen that the most vulnerable position to green water depends on the incident focused wave amplitude, A_f. When A_f is relatively small (approximately less than 0.38 m), the maximum free-surface elevation inside the gap is larger than that in front of the two-box system. However, when A_f becomes larger, the former tends to become lower than the latter. This indicates that the resonant fluid inside the gap has the largest possibility to causing green water when the incident focused wave amplitude is relatively small; conversely, when the incident focused wave amplitude is relatively large, the most vulnerable position shifts to in front of the two-box system. This is different from the related

finding for the steady-state gap resonance induced by regular waves that the maximum free-surface elevation always occurs inside the narrow gap (Jiang et al., 2018; Lu et al., 2011a).

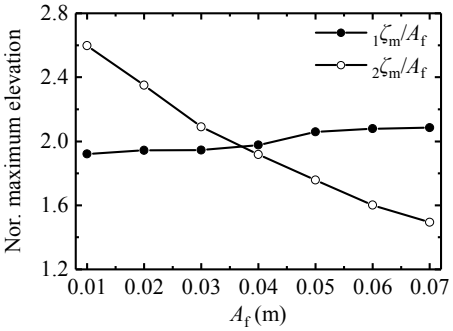

Fig. 9. Comparison of the normalized maximum free-surface elevations at gauges G_1 and G_2 under conditions of various incident focused wave amplitudes

5.2 Response time and damping time of fluid resonance

In actual applications, the accurate and rapid predictions of the response/damping time for the gap resonance phenomenon are vital for the reasonable arrangement of operation time and the safe evacuation of staff. Hence, the response time and the damping time for the transient gap resonance are further investigated in this section. It should be pointed out here that the response time is defined as the time taken from the moment that the fluid just begins to move from rest to the moment that the fluid inside the gap achieves the maximum oscillations, and that the damping time refers to the time taken by the fluid inside the gap decaying from the maximum oscillations to 5% of the maximum oscillations.

Fig. 10 presents the comparison of the time series of the free-surface elevations at the response stage of the transient resonance excited by crest-focused wave groups with various amplitudes. The free-surface elevations in this figure are normalized by their respective maximum values and the horizontal coordinate employed is t-t_m. t_m refers to the moment that the maximum free-surface elevation occurs inside the gap, which is directly obtained from the time series of the free-surface elevation at gauge G_2 for each case. It is clear that the response time is almost identical for all the incident wave groups and is around 8.0 s. This is different from the related finding for the steady-state gap resonance triggered by regular waves that the response time is closely related to the incident wave amplitude and the former decreases gradually with the increase of the latter (Gao et al., 2019b).

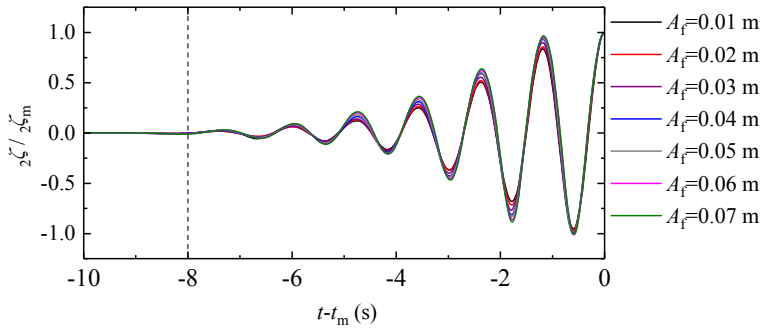

Fig. 10. Comparison of the time series of the free-surface elevations at the response stage of the transient resonance excited by crest-focused wave groups with various amplitudes. The free-surface elevations are normalized by their respective maximum values. t_m in this figure denotes the moment that the maximum free-surface elevation occurs inside the gap.

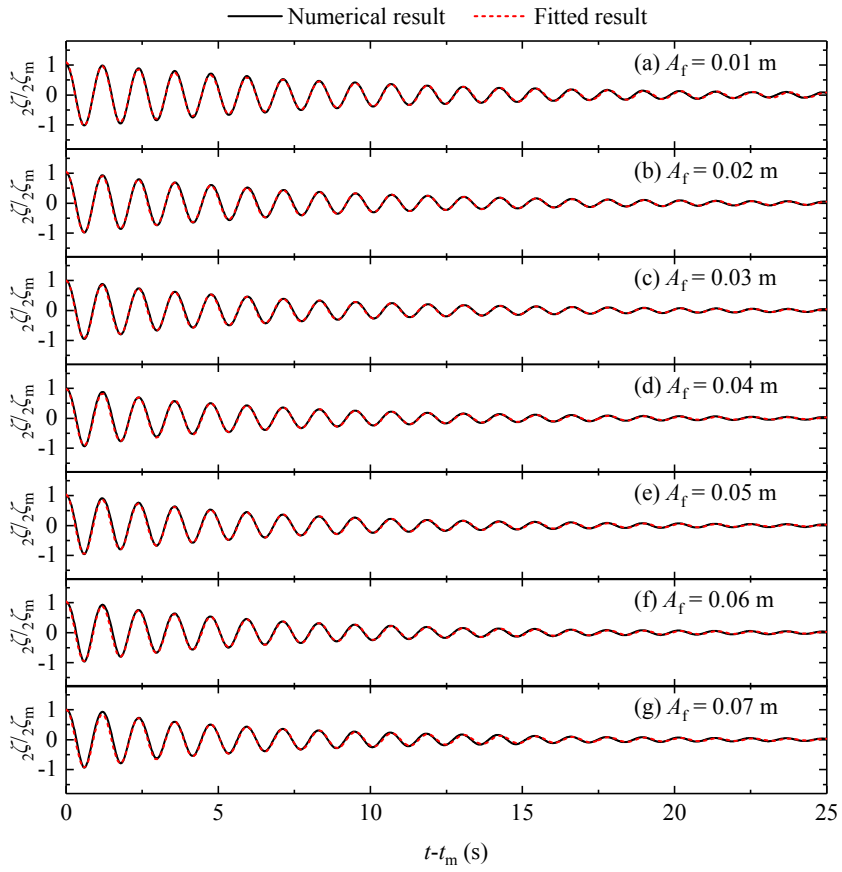

Fig. 11. The damping process of the free-surface elevation inside the gap excited by crest-focused wave groups with various amplitudes. Solid lines and dashed lines denote the simulated free-surface elevations by the numerical model and the fitted ones by Eq. (8).

For the decaying stage of the steady-state gap resonance, it has been found that the envelop of free-surface elevation inside the gap decays in an exponential form (Gao et al., 2019b). Via

carfully observing Fig. 7b and e, it seems that the above-mentioned research finding is also applicable to the transient fluid resonance excited by focused wave groups. To verify this inference, it is assumed that the time series of the free-surface elevations inside the gap at the decaying stage of the transient gap resonance can be expressed as

$$ {}_2\zeta / {}_2\zeta_{\mathrm{m}} = \bar{a}\cos\left[\omega_{\mathrm{m}}\left(t-t_{\mathrm{m}}\right)+\bar{\varphi}\right]\exp\left[-\delta\left(t-t_{\mathrm{m}}\right)\right], \tag{8} $$

where δ is a parameter controlling the damping time of the fluid oscillations and $\bar{a}$ and $\bar{\varphi}$ are another two fitting parameters. In theory, if the fluid oscillations decay from the maximum free-surface elevation perfectly in an exponential form, the values of $\bar{a}$ and $\bar{\varphi}$ are equal to 1 and 0, respectively.

Table 1. Values of various fitting parameters in Eq. (8) and the correlation coefficient, R^2

A_{f} (m)		0.01	0.02	0.03	0.04	0.05	0.06	0.07
Fitted values	$\bar{a}$	1.061	1.054	1.002	0.9980	1.021	1.025	1.008
	$\bar{\varphi}$ (rad)	0.0025	-0.0100	-0.0100	-0.0116	-0.0009	-0.0092	-0.0265
	δ	0.1056	0.1217	0.1308	0.1412	0.1429	0.1434	0.1436
	R^2	0.9931	0.9921	0.9917	0.9905	0.9878	0.9816	0.9745

Fig. 11 illustrates the comparisons of the simulated free-surface elevations inside the gap and the corresponding fitted ones by Eq. (8) during the damping process of the transient fluid resonance. It is seen that for all the incident focused wave groups, the fitted free-surface elevations coincides very well the corresponding simulated ones. Table 1 further lists the values of various fitting parameters and the correlation coefficient, R^2. All the values of $\bar{a}$ and $\bar{\varphi}$ under conditions of all incident wave amplitudes are very close to 1 and 0, respectively. Meanwhile, the correlation coefficients between the simulated and fitted free-surface elevations are all greater than 0.97. All these results presented in Fig. 11 and Table 1 indicate that at the decaying stage of transient gap resonance, the envelop of free-surface elevation inside the gap indeed decays in the exponential form expressed by Eq. (8). In addition, it can be found from Table 1 that the value of δ increases gradually with the increase of A_{f}. As is well known, a larger incident wave amplitude tends to cause more significant energy dissipation caused by the fluid viscosity, vortex shedding and even turbulence during gap resonance (Feng et al., 2017; Gao et al., 2019a). Hence, it can be inferred that the parameter δ depends closely on the energy dissipation of the system, and more

notable energy dissipation corresponds to a larger value of δ.

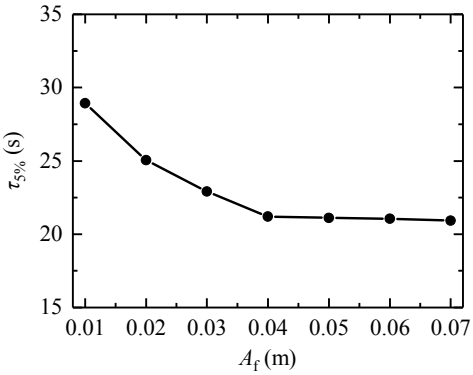

Fig. 12. Damping time of transient fluid oscillations under conditions of various focused wave amplitudes.

Based on the above equation, the time $\tau_{\nu\%}$ needed by the wave to decrease to ν% of the maximum can be further formulated as

$$\tau_{\nu\%} = -\frac{\ln\left[\nu\%/\left(\bar{a}\cos\bar{\varphi}\right)\right]}{\delta}. \tag{9}$$

Identical to Gao et al. (2019b), $\tau_{5\%}$ is selected in this paper to represent the damping time of the resonant free-surface elevations. Fig. 12 presents the damping time of transient fluid oscillations under conditions of various focused wave amplitudes. Two obvious phenomena can be easily observed. First, the damping time for the transient gap resonance decreases gradually with the increase of the focused wave amplitude, which is consistent with the related finding revealed in Gao et al. (2019b) on the damping time for the steady-state gap resonance. Second, the decline rate of the damping time is also shown to gradually decreases with the focused wave amplitude. When A_f increases from 0.01 m to 0.04 m, the damping time decreases significantly from 28.9 s to 21.20 s. However, as A_f increases further from 0.04 m to 0.07 m, the damping time only declines from 21.20 s to 20.91 s.

5.3 Maximum wave loads on each box

5.3.1 Vertical wave forces

Fig. 13 demonstrates the time series of the vertical wave forces on Boxes A and B induced by the crest-focused wave groups with A_f=0.01 m, 0.04 m and 0.07 m. The vertical wave forces in the

figure are normalized by $\rho g h A_f W$. Three phenomena can be clearly observed. First, due to the shielding effect of Box A on Box B, the maximum vertical wave forces on Box B (including in the $+z$- and $-z$-axial directions) are always remarkably less than those acting on Box A at the given frequency. Second, for both boxes, the maximum vertical wave forces in the $-z$-axial direction are always notably greater than the corresponding ones in the $+z$-axial direction. Take A_f=0.04 m for example (see Fig. 13b). The normalized maximum vertical wave forces on Boxes A and B in the $+z$-axial direction are 0.4476 and 0.2547, and those in the $-z$-axial direction increase to 0.5678 and 0.3245, with the growth rates of 27.1% and 27.4%, respectively. Third, at the damping stage, the time series of the vertical wave forces on both boxes gradually become almost identical. This is because the incident focused wave groups has passed away from the two-box system and the remaining large-amplitude piston-like free surface oscillation in the narrow gap can lead to very similar flow velocity and dynamic pressure fields around the bottom of boxes, which leads to the almost identical vertical forces on two boxes (in order to explain this phenomenon intuitively, the distributions of the velocity and dynamic pressure fields around the two-box system at two instants during the damping stage for the crest-focused wave groups with A_f=0.07 m are further illustrated in Fig. 14). Hence, the vertical wave forces on both boxes exerted by the resonant fluid inside the gap are almost identical (including the phase and the magnitude). In addition, it can be expected that the horizontal wave forces and the moments on both boxes exerted by the resonant fluid inside the gap have almost identical magnitude as well but become anti-phase, which will be verified in Sections 5.3.2 and 5.3.3.

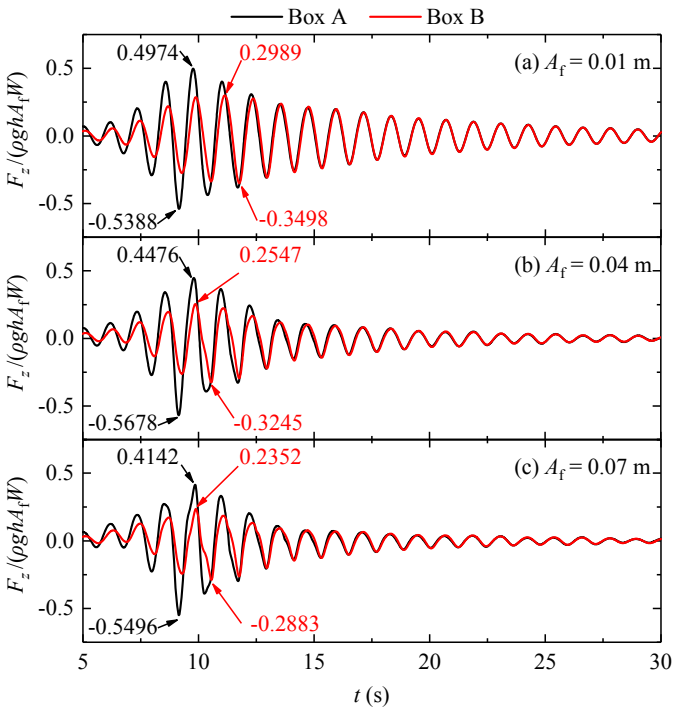

Fig. 13. Time series of the vertical wave forces on Boxes A and B excited by the crest-focused wave groups with A_f=0.01 m, 0.04 m and 0.07 m. The numbers in this figure refer to the values of the maximum vertical wave forces in the +z- or –z-axial directions.

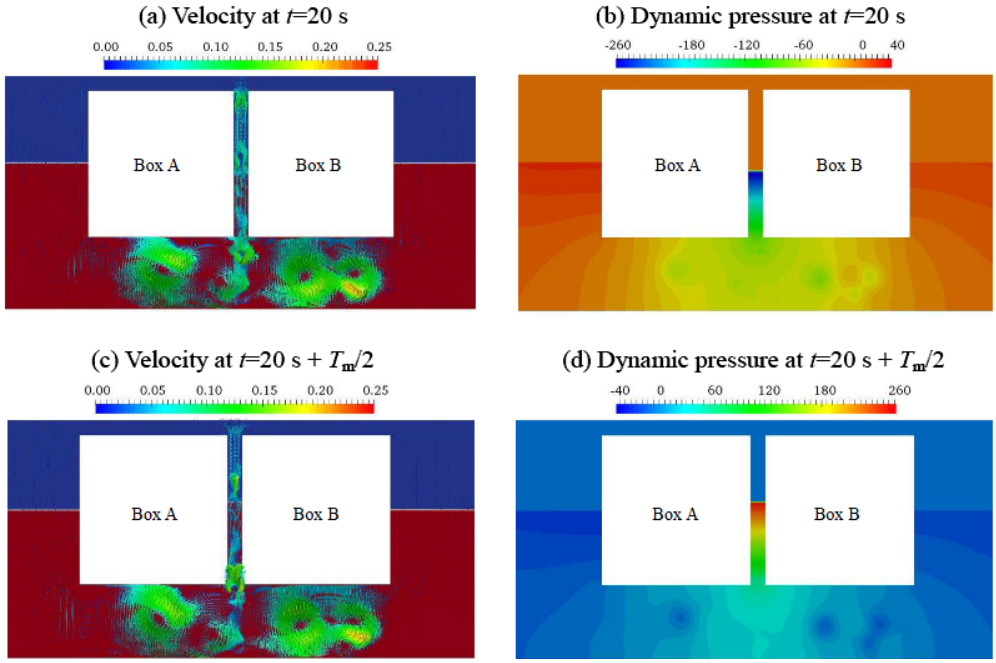

Fig. 14. Distributions of the velocity and dynamic pressure fields around the two-box system at two instants during the damping stage for the crest-focused wave groups with A_f=0.07 m, in which T_m=2π/ω_m refers to the fluid resonant period.

Fig. 15 illustrates the variations of the normalized maximum vertical wave forces on Boxes A and B with respect to the focused wave amplitude. The normalized maximum vertical wave forces on Box A in the +z-axial direction and on Box B in both the +z- and –z-axial directions decrease gradually with the increase of the focused wave amplitude, while those on Box A in the –z-axial direction are shown to fluctuate around 0.55. In addition, the finding in Fig. 13 that the maximum vertical wave forces on Box B are always remarkably less than those on Box A is more intuitively presented in this figure. To further assess how the focused wave amplitude affects the shielding effect of Box A on Box B in term of the maximum vertical wave forces, Fig. 16 shows the ratios of the maximum vertical wave forces on Box B in the +z- and –z-axial directions to the corresponding ones on Box A for all cases. The ratio for the maximum vertical wave forces in the –z-axial direction decreases gradually from 64.9% to 52.4% as A_f increases from 0.01 m to 0.07 m, and the ratio in the +z-axial direction fluctuates between 56.8% and 60.1%. It indicates that, in general, larger focused wave amplitude tends to produce more obvious shielding effect of Box A on Box B in term of the maximum vertical wave forces.

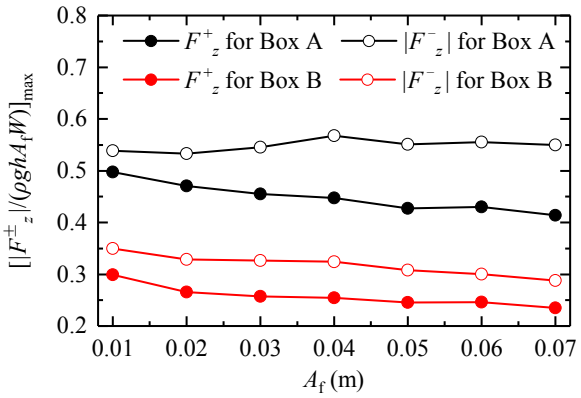

Fig. 15. Normalized maximum vertical wave forces on Boxes A and B for all cases. The superscripts "+" and "–" denote the maximum wave forces in the +z- and –z-axial directions, respectively.

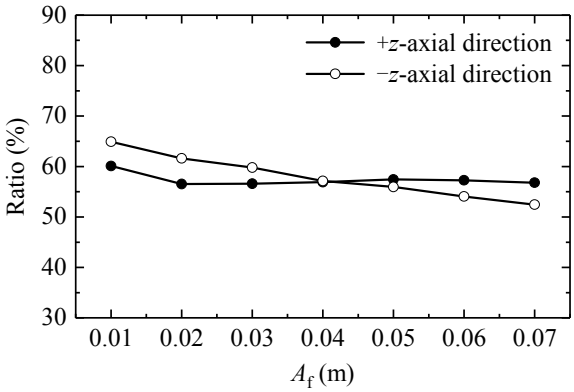

Fig. 16. The ratios of the maximum vertical wave forces on Box B in the +*z*- and –*z*-axial directions to the corresponding ones on Box A for all cases.

5.3.2 Horizontal wave forces

Fig. 17 demonstrates the time series of the horizontal wave forces on Boxes A and B excited by the crest-focused wave groups with A_f=0.01 m, 0.04 m and 0.07 m. Identical to the vertical wave forces, the horizontal wave forces in this figure are also normalized by $\rho g h A_f W$. Compared with the vertical wave forces in Fig. 13, there are both the similar and different phenomena presented in this figure. First, the maximum horizontal wave forces on Box B (including in the +*x*- and –*x*-axial directions) are shown to be always notably less than those on Box A, which is similar to the related finding for the vertical wave forces. Second, for the horizontal forces on Box B, the maximum values in the +*x*-axial direction are always larger than the corresponding maximum ones in the –*x*-axial direction; while for the horizontal forces on Box A, the former becomes less than the latter except when the incident wave group has the largest wave amplitude (i.e., A_f=0.07 m). Third, at the damping stage of the fluid resonance, the time series of the horizontal forces on both boxes have almost identical magnitude but are anti-phase. The last two phenomena described above are different from the corresponding ones shown in Fig. 13.

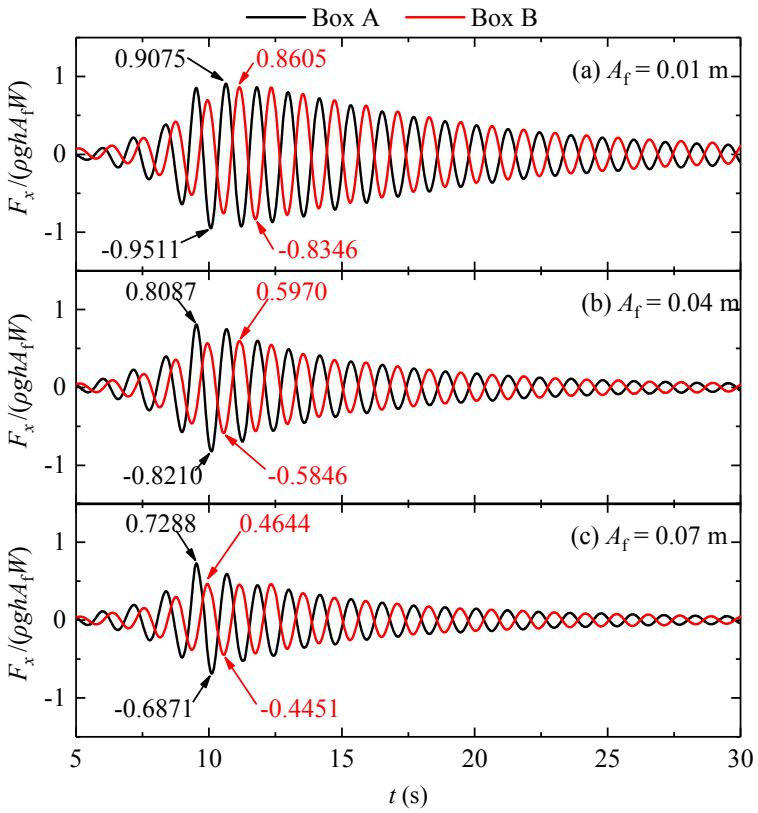

Fig. 17. Time series of the horizontal wave forces on Boxes A and B excited by the crest-focused wave groups with A_f=0.01 m, 0.04 m and 0.07 m. The numbers in this figure refer to the values of the maximum horizontal wave forces in the +x- or –x-axial directions.

Fig. 18 shows the normalized maximum horizontal wave forces on Boxes A and B for all cases. The normalized maximum horizontal wave forces on both boxes and in both directions decrease gradually with the increase of the focused wave amplitude. Besides, the phenomenon in Fig. 17 that the maximum horizontal wave forces on Box B are always notably less than those on Box A is also presented in this figure more directly. To further evaluate how the focused wave amplitude affects the shielding effect of Box A on Box B in term of the maximum horizontal wave forces, the ratios of the maximum horizontal wave forces on Box B in the +x- and –x-axial directions to the corresponding ones on Box A for all cases are illustrated in Fig. 19. Their ratios in both the +x- and –x-axial directions are shown to decreases gradually with the focused wave amplitude, which indicates that larger focused wave amplitude leads to more pronounced shielding effect of the upstream box on the downstream one in term of the maximum horizontal wave forces in both the +x- and –x-axial directions.

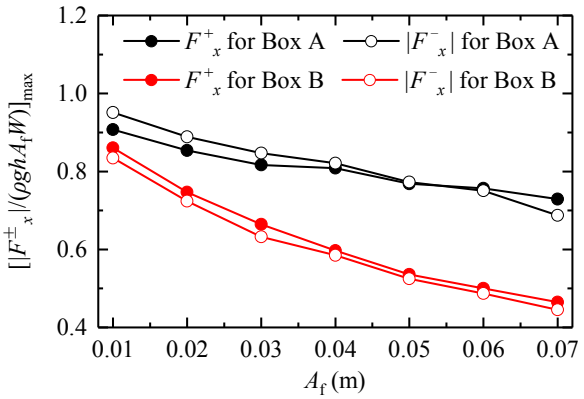

Fig. 18. Normalized maximum horizontal wave forces on Boxes A and B for all cases. The superscripts "+" and "–" denote the maximum wave forces in the +*x*- and –*x*-axial directions, respectively.

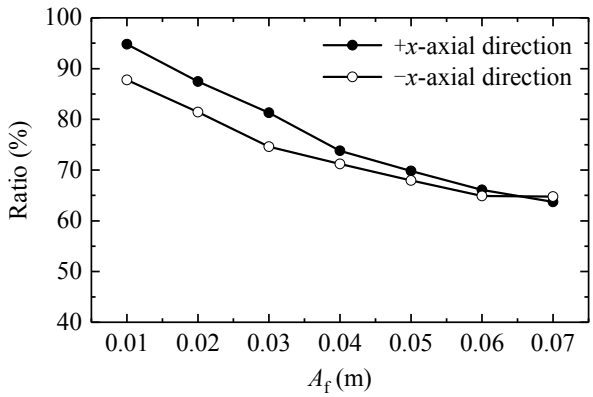

Fig. 19. The ratios of the maximum horizontal wave forces on Box B in the +*x*- and –*x*-axial directions to the corresponding ones on Box A for all cases.

5.3.3 Wave moments

Fig. 20 presents the time series of the moments on Boxes A and B induced by the crest-focused wave groups with A_f=0.01 m, 0.04 m and 0.07 m, in which the moments are normalized by $\rho g h A_f B W$. Three phenomena can be clearly seen. First, the maximum moments on Box B (including in the +*y*- and –*y*-axial directions) are always remarkably lower than those on Box A, which is similar to the related findings for both the maximum vertical and horizontal wave forces. Second, for Box A, the maximum moments in the +*y*-axial direction are always larger than the corresponding ones in the –*y*-axial direction, while for Box B, the former becomes

significantly less than the latter. This phenomenon is not exactly the same as neither the vertical nor the horizontal wave forces. Third, similar to the horizontal wave forces, the time series of the moments on both boxes have almost identical magnitude but are anti-phase at the damping stage of the fluid resonance.

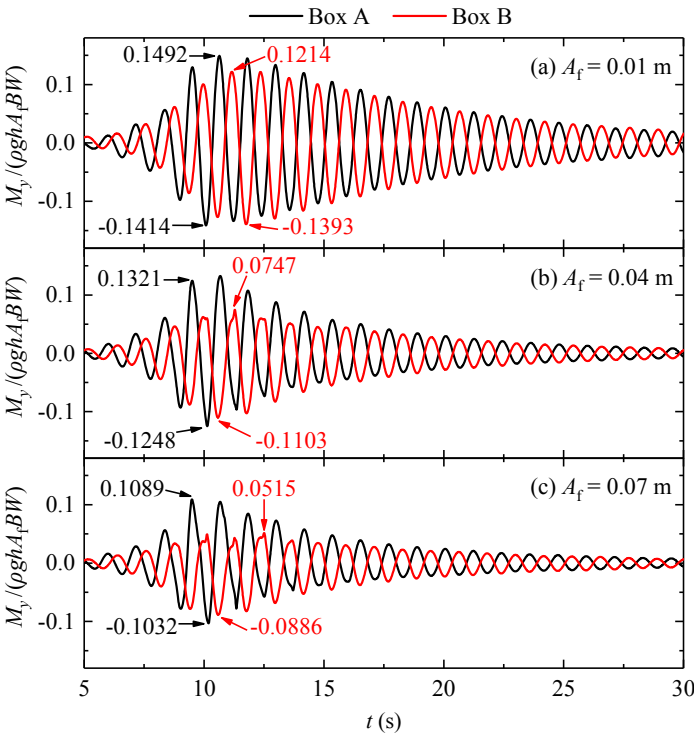

Fig. 20. Time series of the moments on Boxes A and B induced by the crest-focused wave groups with A_f=0.01 m, 0.04 m and 0.07 m.

Fig. 21 shows the variations of the normalized maximum moments on Boxes A and B with respect to the focused wave amplitude. Similar to the maximum horizontal wave forces in Fig. 18, the normalized maximum moments on both boxes and in both directions decrease gradually with the focused wave amplitude. In addition, this figure more visually displays the finding in Fig. 20 that the maximum moments on Box B are always remarkably lower than those on Box A. The ratios of the maximum moments on Box B in the +y- and –y-axial directions to the corresponding ones on Box A for all cases are further demonstrated in Fig. 22. At the range of 0.01 m ≤ A_f ≤0.06 m, the ratios of the maximum moments in both the +y-axial and –y-axial directions decreases monotonously with the increase of the focused wave amplitude. As A_f further increases from 0.06 m to 0.07 m, the ratios of the maximum moments in both directions is only slightly increased. This

illustrates that larger focused wave amplitude tends to cause more obvious shielding effect of the upstream box on the downstream one in term of the maximum moments in both the +*y*- and –*y*-axial directions overall.

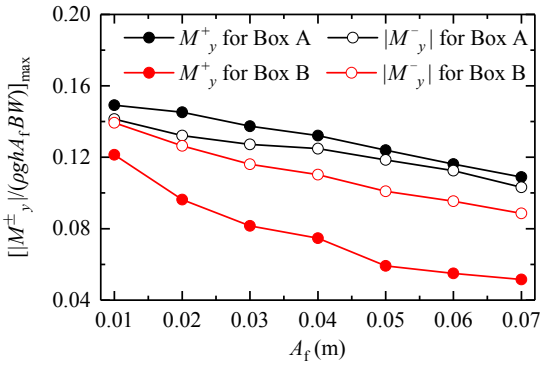

Fig. 21. Normalized maximum moments on Boxes A and B for all cases. The superscripts "+" and "–" denote the maximum moments in the +*y*- and –*y*-axial directions, respectively.

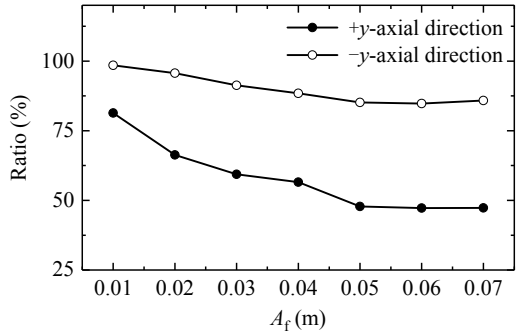

Fig. 22. The ratios of the maximum moments on Box B in the +*y*- and –*y*-axial directions to the corresponding ones on Box A for all cases.

Hence, based on the phenomena shown in Figs. 13-22, the following main conclusions on the maximum wave loads (including the maximum vertical wave forces, the maximum horizontal wave forces and the maximum moments) during the transient gap resonance can be drawn. First, the maximum wave loads on Box B are always remarkably lower than the corresponding ones on Box A. Second, the normalized maximum wave loads on both boxes decrease gradually with the increase of the focused wave amplitude overall. Third, in general, larger focused wave amplitude tends to bring about more obvious shielding effect of the upstream box on the downstream one in term of the maximum wave loads.

5.4 Higher-order wave loads

As mentioned in Section 3, the four-phase combination method proposed by Fitzgerald et al. (2014) is utilized to assess the relative importance of the higher-order wave loads to the first-order ones during transient gap resonance. Based on this method, the separation of a total wave force into the first four order components can be achieved by controlling the phase of incident focused waves (e.g. Chen et al. (2019); Fitzgerald et al. (2014)). In this article, the separated second-, third- and fourth-order components of wave loads are added up and their summation is termed as "higher-order wave loads". It should be stressed here that the second-order difference-frequency components is also included in the higher-order wave loads.

Fig. 23 presents the time series of the first- and the higher-order vertical wave forces on Boxes A and B under condition of A_f=0.04 m. For the first-order components on both boxes (see Fig. 23a and c), the maximum wave forces in the +z-axial direction are almost identical to the corresponding ones in the –z-axial direction. The normalized maximum first-order wave forces in the +z- and –z-axial directions on Box A are 0.4803 and 0.4819, respectively, and those on Box B are 0.2572 and 0.2576, respectively. Different from the first-order components, the higher-order vertical wave forces presents the obvious asymmetry on their maximums in both directions (see Fig. 23 b and d). The normalized maximum higher-order vertical wave forces in the +z- and –z-axial directions on Box A are 0.0421 and 0.0922, respectively, and those on Box B are 0.0517 and 0.0808, respectively. It reflects the strong nonlinearity of the higher-order wave loads.

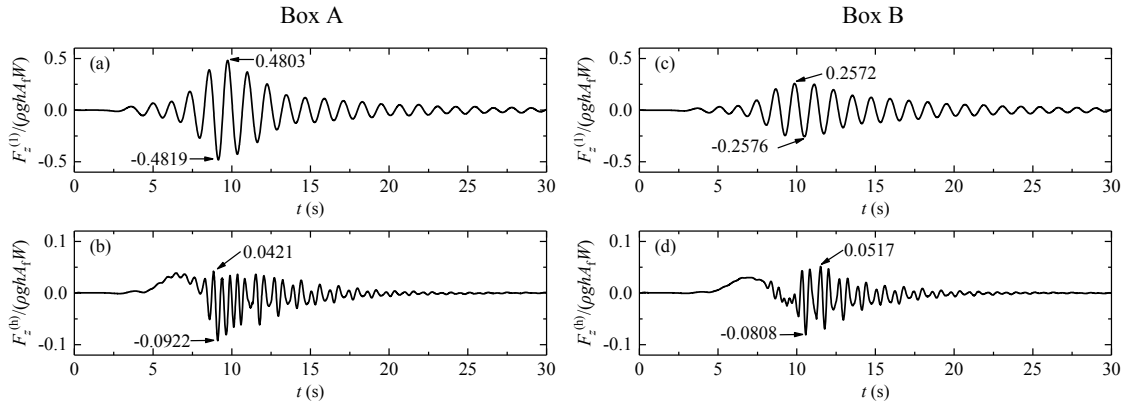

Fig. 23. Time series of the first- and the higher-order vertical wave forces on Boxes A and B under condition of A_f=0.04 m. (a) and (b) correspond to Box A; (c) and (d) correspond to Box B. The superscripts "(1)" and "(h)" denote the first- and the higher-order wave forces, respectively.

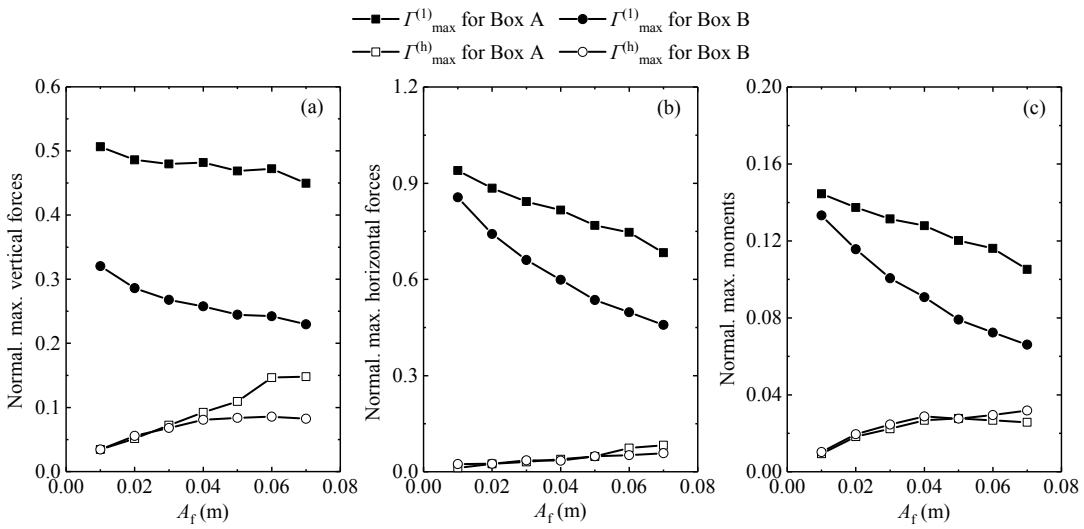

Fig. 24. Normalized first- and higher-order wave loads acting on both boxes for all cases. (a)-(c) correspond to the vertical forces, horizontal forces and moments, respectively.

Fig. 24 presents the variations of the normalized first- and higher-order wave loads acting on both boxes with respect to the incident focused wave amplitude, A_f. The symbol "Γ" in this figure represents the vertical wave force, the horizontal wave force or the moment on both boxes. $\Gamma^{(1)}_{max}$ and $\Gamma^{(h)}_{max}$ respectively denote the normalized first- and higher-order wave loads, which are defined as:

$$\Gamma^{(1)}_{max} = \max\left(\Gamma^{(1)+}_{max}, \left|\Gamma^{(1)-}_{max}\right|\right), \tag{10}$$

and

$$\Gamma^{(h)}_{max} = \max\left(\Gamma^{(h)+}_{max}, \left|\Gamma^{(h)-}_{max}\right|\right). \tag{11}$$

$\Gamma^{(1)+}_{max}$, $\Gamma^{(1)-}_{max}$, $\Gamma^{(h)+}_{max}$ and $\Gamma^{(h)-}_{max}$ denote the normalized maximum first- and higher-order wave loads in the corresponding positive and negative axial directions, which can be obtained directly from the time series of the first- and higher-order wave loads (refer to the numbers marked in Fig. 23). There are three obvious phenomena that can be seen from this figure. First, the normalized first-order wave loads decrease gradually with A_f, while the normalized higher-order ones are shown to increase with A_f overall. Second, the first-order wave loads on Box A are always significantly larger than the corresponding first-order ones on Box B. Third, for both the higher-order horizontal wave forces and moments (Fig. 24b and c), their values on both boxes are presented to be always very close to each other. While for the higher-order vertical wave forces (Fig. 24a), the similarity of their values on both boxes is available only when $A_f \leq 0.3$ m. As A_f

increases further, the higher-order vertical forces on Box A become obviously higher than the corresponding ones on Box B.

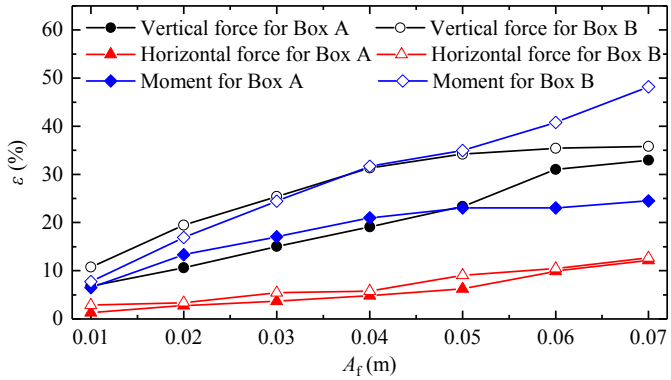

Fig. 25. Amplitude ratios of the higher-order components to the first-order components for the vertical wave forces, the horizontal wave forces and the moments on Boxes A and B under conditions of various focused wave amplitudes.

In this article, the amplitude ratio of the higher-order wave loads to the first-order ones is defined as

$$\varepsilon = \frac{\Gamma_{\max}^{(\mathrm{h})}}{\Gamma_{\max}^{(1)}} \times 100\% , \tag{12}$$

Obviously, the amplitude ratio, ε, can measure the relative importance of the higher-order wave loads to the first-order ones quantitatively. Fig. 25 demonstrates the amplitude ratios of the higher-order components to the first-order components for the three kinds of wave loads (i.e., the vertical wave forces, the horizontal wave force and the moment) on Boxes A and B under conditions of various focused wave amplitudes. The following three phenomena can be clearly seen. First, for all the three kinds of wave loads on both boxes, their amplitude ratios, ε, are shown to increase monotonously with the increase of the focused wave amplitude. Take the wave loads on Box B for example. As A_f rises from 0.01 m to 0.07 m, the values of ε for the horizontal wave force, the vertical wave force and the moment increase from 2.8%, 10.8% and 7.7% to 12.7%, 35.8% and 48.2%, respectively. This means that with the rise of the focused wave amplitude, the higher-order wave loads become more and more remarkable compared with the first-order ones. Second, for all the focused wave amplitudes considered, the amplitude ratios, ε, for the vertical wave forces and the moments are significantly greater than those for the horizontal wave forces.

Third, for all the three kinds of wave load (especially for the vertical force and the moment), the values of ε for Box B are always obviously larger than the corresponding ones for Box A.

6. Conclusions

The viscous flow model OpenFOAM® combined with the "*waves2Foam*" toolbox is adopted in this article to study the hydrodynamic characteristics of the transient gap resonance in a narrow gap between two fixed boxes triggered by focused wave groups with various focused wave amplitudes. The wave climates not only inside the gap but in the vicinity of the two-box system, the response time and the damping time of the transient gap resonance, the maximum wave loads on both boxes and the relative importance of the higher-order wave loads to the first-order ones are comprehensively investigated. The results of the current research have provided new insights of the hydrodynamic characteristics involved in the transient gap resonance excited by focused wave groups.

The following conclusions can be drawn from the results of the present study:

1. The amplification factor of the free-surface elevation in front of the two-box system increases monotonously with the increase of the focused wave amplitude, while the former both inside the gap and at the rear of the system is shown to decrease gradually with the latter. From the viewpoint of causing green water on the deck, the transmitted wave group at the rear of the system has the least possibility. As for the other two positions (i.e, inside the gap and in front of the system), the most vulnerable position to occurring green water closely depends on the incident focused wave amplitude, A_{f}. When A_{f} is relatively small, the most vulnerable position is located inside the gap; when A_{f} is relatively large, the most vulnerable position shifts to in front of the system.
2. The response time of the transient fluid resonance from the moment that the fluid just begins to move from rest to the moment that the fluid achieves the maximum oscillations is almost identical for all the focused wave groups considered. At the decaying stage of the transient resonance, the envelop of free-surface elevation inside the gap is found to decay in an exponential form. The damping time decreases gradually with the increase of the focused wave amplitude, and the decline rate of the former also decreases gradually with the latter.
3. For the maximum wave loads (including the maximum vertical wave forces, the maximum

horizontal wave forces and the maximum moments), it is shown that the maximum wave loads on Box B are always remarkably lower than the corresponding ones on Box A. The normalized maximum wave loads on both boxes decrease gradually with the focused wave amplitude overall. In addition, in term of the maximum wave loads, larger focused wave amplitude tends to bring about more obvious shielding effect of the upstream box on the downstream one.

4. The relative importance of the higher-order wave loads to the first-order ones becomes more and more remarkable as the incident focused wave amplitude increases, and their amplitude ratios, ε, may reach up to nearly 50% under condition of the largest focused wave amplitude considered. The relative importance of the higher-order wave loads for the vertical wave force and the moment are significantly greater than that for the horizontal wave force. In addition, the relative importance of the higher-order wave loads for Box B is obviously greater than that for Box A, especially for the vertical wave force and the moment.

Finally, we reaffirm here that these conclusions are only valid for the given geometrical layout (including the water depth, the gap width and the size and draft of the two boxes), the given spatial focused position (i.e., at the middle of the narrow gap) and the variation range of the incident focused wave amplitude studied in this article.

Acknowledgments

This research is financially supported by the National Key Research and Development Program (2017YFC1404200), the National Natural Science Foundation of China (Grant Nos. 51911530205, 51609108, 51809039 and 51709136) and the Science Foundation from the Education Department of Jilin Province of China (Grant No. JJKH20180452KJ). The authors also thank UK EPSRC (Grant No. EP/R007519/1), the Royal Academy of Engineering (Grant No. UK-CIAPP/73) and the Royal Society (Grant No. IEC\NSFC\181321) for providing partial support for this work.

References

Chen, L.F., Stagonas, D., Santo, H., Buldakov, E.V., Simons, R.R., Taylor, P.H., Zang, J., 2019.

Numerical modelling of interactions of waves and sheared currents with a surface piercing vertical cylinder. Coastal Engineering 145, 65-83.

Chen, L.F., Zang, J., Hillis, A.J., Morgan, G.C.J., Plummer, A.R., 2014. Numerical investigation of wave-structure interaction using OpenFOAM. Ocean Engineering 88, 91-109.

Chua, K.H., Taylor, R.E., Choo, Y.S., 2018. Hydrodynamic interaction of side-by-side floating bodies part I: Development of CFD-based numerical analysis framework and modified potential flow model. Ocean Engineering 166, 404-415.

Feng, X., Bai, W., 2015. Wave resonances in a narrow gap between two barges using fully nonlinear numerical simulation. Applied Ocean Research 50, 119-129.

Feng, X., Bai, W., Chen, X.B., Qian, L., Ma, Z.H., 2017. Numerical investigation of viscous effects on the gap resonance between side-by-side barges. Ocean Engineering 145, 44-58.

Fernández, H., Sriram, V., Schimmels, S., Oumeracic, H., 2014. Extreme wave generation using self correcting method - Revisited. Coastal Engineering 93, 15-31.

Fitzgerald, C.J., Taylor, P.H., Taylor, R.E., Grice, J., Zang, J., 2014. Phase manipulation and the harmonic components of ringing forces on a surface-piercing column. Proceedings of the Royal Society London A: Mathematical, Physical & Engineering Sciences 470 (2168), 20130847.

Gao, J., He, Z., Zang, J., Chen, Q., Ding, H., Wang, G., 2019a. Topographic effects on wave resonance in the narrow gap between fixed box and vertical wall. Ocean Engineering 180, 97-107.

Gao, J., He, Z., Zang, J., Chen, Q., Ding, H., Wang, G., 2020a. Numerical investigations of wave loads on fixed box in front of vertical wall with a narrow gap under wave actions. Ocean Engineering 206, 107323.

Gao, J., Ma, X., Zang, J., Dong, G., Ma, X., Zhu, Y., Zhou, L., 2020b. Numerical investigation of harbor oscillations induced by focused transient wave groups. Coastal Engineering 158, 103670.

Gao, J., Zang, J., Chen, L., Chen, Q., Ding, H., Liu, Y., 2019b. On hydrodynamic characteristics of gap resonance between two fixed bodies in close proximity. Ocean Engineering 173, 28-44.

Hasselmann, K., Barnett, T.P., Bouws, E., Carlson, H., Cartwright, D.E., Enke, K., Ewing, J.A., Gienapp, H., Hasselmann, D.E., Kruseman, P., Meerburg, A., Müller, P., Olbers, D.J., Richter,

K., Sell, W., Walden, H., 1973. Measurements of wind-wave growth and swell decay during the Joint North Sea Wave Project (JONSWAP). Dtsch. Hydrogr. Z A8, 1–95.

Huang, X.H., Xiao, W., Yao, X.L., Gu, J.Y., Jiang, Z.Y., 2020. An experimental investigation of reduction effect of damping devices in the rectangular moonpool. Ocean Engineering 196, 106767.

Huijsmans, R.H.M., Pinkster, J.A., Wilde, J.J.d., 2001. Diffraction and radiation of waves around side-by-side moored vessels, Proceedings of the Eleventh (2001) International Offshore and Polar Engineering Conference, Stavanger, Norway. Paper No. ISOPE-I-01-061., pp. 406-412.

Jacobsen, N.G., Fuhrman, D.R., Fredsøe, J., 2012. A wave generation toolbox for the open-source CFD library: OpenFoam®. International Journal for Numerical Methods in Fluids 70 (9), 1073-1088.

Ji, C.-Y., Chen, X., Cui, J., Gaidai, O., Incecik, A., 2016. Experimental study on configuration optimization of floating breakwaters. Ocean Engineering 117, 302-310.

Jiang, S.-C., Bai, W., Cong, P.-W., Yan, B., 2019a. Numerical investigation of wave forces on two side-by-side non-identical boxes in close proximity under wave actions. Marine Structures 63, 16-44.

Jiang, S.-C., Bai, W., Tang, G.-Q., 2018. Numerical simulation of wave resonance in the narrow gap between two non-identical boxes. Ocean Engineering 156, 38-60.

Jiang, S.-C., Bai, W., Tang, G., 2019b. Numerical investigation of piston-modal wave resonance in the narrow gap formed by a box in front of a wall. Physics of Fluids 31, 052105.

Johannessen, T.B., Swan, C., 2008. A laboratory study of the focusing of transient and directionally spread surface water waves. Royal Society of London Proceedings Series A 457, 971-1006.

Li, B., Cheng, L., J.Deeks, A., Teng, B., 2005. A modified scaled boundary finite-element method for problems with parallel side-faces. Part II. Application and evaluation. Applied Ocean Research 27 (4-5), 224-234.

Li, X., Xu, L.-y., YANG, J.-m., 2016. Study of fluid resonance between two side-by-side floating barges. Journal of Hydrodynamics, Ser. B 28 (5), 767-777.

Li, Y., 2019. Fully nonlinear analysis of second-order gap resonance between two floating barges. Engineering Analysis with Boundary Elements 106, 1-19.

Li, Y., Zhang, C., 2016. Analysis of wave resonance in gap between two heaving barges. Ocean Engineering 117, 210-220.

Lu, L., Teng, B., Cheng, L., Sun, L., Chen, X., 2011a. Modelling of multi-bodies in close proximity under water waves—Fluid resonance in narrow gaps. Science China Physics, Mechanics and Astronomy 54 (1), 16-25.

Lu, L., Teng, B., Sun, L., Chen, B., 2011b. Modelling of multi-bodies in close proximity under water waves—Fluid forces on floating bodies. Ocean Engineering 38 (13), 1403-1416.

Miao, G., Ishida, H., Saitoh, T., 2000. Influence of gaps between multiple floating bodies on wave forces. China Ocean Engineering 14 (4), 407-422.

Molin, B., 2001. On the piston and sloshing modes in moonpools. Journal of Fluid Mechanics 430, 27-50.

Ning, D., Su, X., Zhao, M., Teng, B., 2015a. Hydrodynamic difference of rectangular-box systems with and without narrow gaps. Journal of Engineering Mechanics 141 (8), 04015023.

Ning, D., Su, X., Zhao, M., Teng, B., 2015b. Numerical study of resonance induced by wave action on multiple rectangular boxes with narrow gaps. Acta Oceanologica Sinica 34 (5), 92-102.

Saitoh, T., Miao, G., Ishida, H., 2006. Theoretical analysis on appearance condition of fluid resonance in a narrow gap between two modules of very large floating structure, Proceedings of the 3rd Asia-Pacific Workshop on Marine Hydrodynamics, Shanghai, China, pp. 170-175.

Sun, L., Taylor, R.E., Taylor, P.H., 2010. First- and second-order analysis of resonant waves between adjacent barges. Journal of Fluids and Structures 26 (6), 954-978.

Tan, L., Lu, L., Liu, Y., Sabodash, O.A., Teng, B., 2014. Dissipative Effects of Resonant Waves in Confined Space Formed by Floating Box in Front of Vertical Wall, Proceedings of the Eleventh ISOPE Pacific/Asia Offshore Mechanics Symposium, Shanghai, China. Paper No. ISOPE-P-14-080.

Tan, L., Lu, L., Tang, G.-Q., Cheng, L., Chen, X.-B., 2019. A viscous damping model for piston mode resonance. Journal of Fluid Mechanics 871, 510-533.

Taylor, R.E., Sun, L., Taylor, P.H., 2008. Gap resonances in focused wave groups, Proceedings of the 23rd International Workshop on Water Waves and Floating Bodies, Jeju, Korea.

Tromans, P.S., Anaturk, A.R., Hagemeijer, P., 1991. A new model for the kinematics of large ocean

waves - application as a design wave, The First International Offshore and Polar Engineering Conference. International Society of Offshore and Polar Engineers (ISOPE), Edinburgh.

Wang, H., Draper, S., Zhao, W., Wolgamot, H., Cheng, L., 2018. Development of a computational fluid dynamics model to simulate three-dimensional gap resonance driven by surface waves. Journal of Offshore Mechanics and Arctic Engineering 140, 061803.

Wang, H., Wolgamot, H.A., Draper, S., Zhao, W., Taylor, P.H., Cheng, L., 2019. Resolving wave and laminar boundary layer scales for gap resonance problems. Journal of Fluid Mechanics.

Zhao, W., Wolgamot, H.A., Taylor, P.H., Taylor, R.E., 2017. Gap resonance and higher harmonics driven by focused transient wave groups. Journal of Fluid Mechanics 812, 905-939.

Zhao, X., Ning, D., 2018. Experimental investigation of breakwater-type WEC composed of both stationary and floating pontoons. Energy 155, 226-233.

Zhu, R., Miao, G., You, Y., 2005. Influence of gaps between 3-D multiple floating structures on wave forces. Journal of Hydrodynamics, Ser. B 17 (2), 141-147.